nature communications

Article

https://doi.org/10.1038/s41467-024-53437-5

Ultrahigh thermal stability and piezoelectricity of lead-free KNN-based texture piezoceramics

Received: 20 June 2024

Accepted: 12 October 2024

Published online: 18 October 2024

Check for updates

Lihui Xu[1,7], Jinfeng Lin[1,7], Yuxuan Yang[2,7], Zhihao Zhao[2], Xiaoming Shi[3], Guanglong Ge[1], Jin Qian[1], Cheng Shi[1], Guohui Li[1], Simin Wang[1], Yang Zhang[2], Peng Li[4], Bo Shen[1] ✉, Zhengqian Fu[5], Haijun Wu[2] ✉, Houbing Huang[6] ✉, Fei Li[2], Xiangdong Ding[2], Jun Sun[2] & Jiwei Zhai[1] ✉

The contradiction between high piezoelectricity and uniquely poor temperature stability generated by polymorphic phase boundary is a huge obstacle to high-performance (K, Na)NbO_3 -based ceramics entering the application market as Pb-based substitutes. We possess the phase boundary by mimicking Pb(Zr, Ti)O_3's morphotropic phase boundary structure via the synergistic optimization of diffusion phase boundary and crystal orientation in $0.94(Na_{0.56}K_{0.44})NbO_3$–$0.03Bi_{0.5}Na_{0.5}ZrO_3$–$0.03(Bi_{0.5}K_{0.5})HfO_3$ textured ceramics. As a result, a prominent comprehensive performance is obtained, including giant d_{33} of 550 ± 30 pC/N and ultrahigh temperature stability (d_{33} change rate less than 1.2% within 25-150 °C), representing a significant breakthrough in lead-free piezoceramics, even surpassing the Pb-based piezoelectric ceramics. Within the same temperature range, the d_{33} change rate of the commercial Pb(Zr, Ti)O_3–5 ceramics is only about 10%, and more importantly, its d_{33} (~ 350 pC/N) is much lower than that of the (K, Na)NbO_3-based ceramics in this work. This study demonstrates a strategy for constructing the phase boundary with MPB feature, settling the problem of temperature instability in (K, Na)NbO_3-based ceramics.

Piezoceramics can achieve the conversion of mechanical energy and electrical energy, endowing electromechanical devices with the function of energy conversion. The salient permittivity and piezoelectric constant adjacent to the morphotropic phase boundary (MPB) determine that lead zirconate titanate (Pb(Zr, Ti)O_3, PZT)-based piezoceramics have dominated the piezoceramics market[1,2]. In response to the call for environmental protection and sustainable development, it is urgent to develop competitive lead-free counterparts. Among several well-known lead-free piezoceramics, potassium sodium niobate (KNN) based ceramics with both high piezoelectric properties and Curie temperature have sparked a research boom[3–6]. However, the comprehensive performance of pure KNN ceramic is far from comparable to lead-based piezoceramics, and tremendous efforts have been made to narrow the gap between them[7–10].

Drawing on the experience of the MPB construction in lead-based ceramics, similarly, polymorphic phase boundary (PPB) was successfully constructed in KNN-based ceramics to improve the piezoelectric performance[11–15]. To date, four main phase boundaries (Rhombohedral

[1]School of Materials Science and Engineering, Tongji University, Shanghai, China. [2]State Key Laboratory for Mechanical Behavior of Materials, Xi'an Jiaotong University, Xi'an, PR China. [3]Department of Physics, University of Science and Technology Beijing, Beijing, China. [4]School of Materials Science and Engineering, Liaocheng University, Liaocheng, China. [5]Chinese Acad Sci, Shanghai Inst Ceram, State Key Lab High Performance Ceram & Superfine, Shanghai, China. [6]School of Materials Science and Engineering, Beijing Institute of Technology, Beijing, China. [7]These authors contributed equally: Lihui Xu, Jinfeng Lin, Yuxuan Yang. ✉e-mail: shenbo@tongji.edu.cn; wuhaijunnavy@xjtu.edu.cn; hbhuang@bit.edu.cn; apzhai@tongji.edu.cn

- Orthorhombic, Orthorhombic - Tetragonal, Rhombohedral - Tetragonal, Rhombohedral - Orthorhombic - Tetragonal) have been obtained at room temperature in KNN-based piezoceramics. Researchers represented by Wu et al. have successfully surpassed the d_{33} of KNN-based ceramics by 600 pC/N based on the PPB construction, greatly stimulating the enthusiasm of researchers[16–18]. However, it is worth noting that MPB in lead-based systems is essentially a composition-driven phase boundary that is virtually independent of temperature, whereas PPB shows a clear temperature dependence. Thereby, by suffering from polycrystalline phase boundaries, these state-of-the-art KNN-based ceramics exhibit severe temperature instability of the d_{33}[19]. Generally, not only the high piezoelectric coefficient but also the corresponding stability over temperature range of −20 to 140 °C are crucial for practical applications. How to simultaneously improve the piezoelectricity and its temperature stability in one sample becomes a pivotal issue for KNN-based ceramics. Hence, the construction of traditional PPB, accompanied by abrupt phase transition, is far from meeting the requirements for improving the comprehensive performance of KNN-based ceramics.

In recent years, PPB with a relatively diffused phase transition at room temperature has been discovered. The presence of diffused PPB alleviates the significant performance fluctuations near the phase transition. Therefore, researchers attempt to modulate PPB in KNN-based ceramics through various strategies, transforming it from a temperature-sensitive traditional PPB to a temperature-insensitive diffused PPB[20–28]. For example, Li et al. utilized $CaZrO_3$ doping to obtain relatively diffused phase transition characteristics at room temperature, resulting in the strain varying less than 10% in the temperature regime from room temperature up to 175 °C[27]. Through the multiphase coexistence strategy, Xi et al. also achieved the same trend of change in the piezoelectric constant (d_{33}) and dielectric constant of KNN-based ceramics within certain temperature range, breaking the bottleneck of its high temperature dependence[29]. Subsequently, researchers have found that constructing composition-driven successive and diffused phase boundaries is also an efficient method to improve the temperature stability of the piezoelectric coefficient. For instance, Wu et al. pioneered the construction of diffused PPT by designing compositionally graded composites, achieving an excellent d_{33} change rate of 6% within the temperature range of 25–100 °C and the d_{33} change rate of 25% in the range of 25–150 °C. Although its piezoelectric coefficient was not satisfactory enough (~350 pC/N), this study laid an important foundation for improving the temperature stability of KNN-based ceramics[30,31]. The discovery of PPB with diffused phase transition characteristics has brought dawn to KNN-based ceramics with high piezoelectric performance to achieve temperature independence. However, there is still a certain discrepancy between diffused PPB and MPB, which urgently requires us to address this issue.

Inspired by the above considerations, we urgently need to develop a kind of KNN-based ceramics with excellent comprehensive performance to mitigate the inconsistency of high d_{33} and its temperature stability. In view of the great advantages of texture technology in significantly increasing the d_{33} and the temperature independence of domains, we are eager to solve the above problems by adopting both strategies simultaneously to mimic PZT's MPB structure in KNN-based textured ceramics, albeit difficult to realize[19,25–27,32–36]. Hence, a new-type phase boundary with MPB feature was constructed to solve this puzzle in this work, which is achieved by introducing $(Bi_{0.5}K_{0.5})HfO_3$ into the $0.97(Na_{0.56}K_{0.44})NbO_3$–$0.03Bi_{0.5}Na_{0.5}ZrO_3$ matrix and simultaneously introducing texture technology, where $Bi^{3+}$and Hf^{4+} contribute to the formation of O-T coexisting phase boundary[29,34]. It is expected that this kind of phase boundary with MPB feature will adjust the stability of d_{33} over a wide temperature range, as the fluctuation of the piezoelectric coefficient d_{33} with temperature variation caused by the conventional abrupt polymorphic phase transition will be preliminarily suppressed to some extent. Meanwhile, the $<00l>_C$ crystal orientation induced by texture technology and the construction of the O-T phase boundary can also greatly promote the polarization switching of piezoelectric materials, significantly improving their piezoelectric performance. Therefore, we successfully obtained ultra-high temperature stability of d_{33} (the change rate less than 1.2% within the temperature range of 25–150 °C and less than 10% within 25–250 °C) and piezoelectric coefficient (d_{33}~550 ± 30 pC/N) in the $(0.97\text{-}x)(Na_{0.56}K_{0.44})NbO_3$–$0.03Bi_{0.5}Na_{0.5}ZrO_3$-$x(Bi_{0.5}K_{0.5})HfO_3$ (KNN-BNZ-xBKH) textured ceramics. This work provides a key approach for the development of practical lead-free KNN-based piezoelectric ceramics (Fig. 1).

Results and discussion

Formation of crystal orientation and phase boundary with MPB feature

The SEM images of the KNN-BNZ-xBKH ceramics are shown in Fig. S1. Notably, it can be seen that the textured ceramics (abbreviated as xT) exhibit typical brick-wall-like grains aligned parallel to the tape-casting plane, and the grain size is significantly larger than that of random ceramics (abbreviated as xR). The large grains of the textured ceramics (~20–30 μm) are close to the size of NN templates (Fig. S2), indicating that the NN seed templates act as a nucleation site during grain growth. In addition, as a representative component of electrical properties, the energy-dispersive spectroscopy (EDS) analysis also shows that the element distribution in 3T ceramics is uniform and there are no other

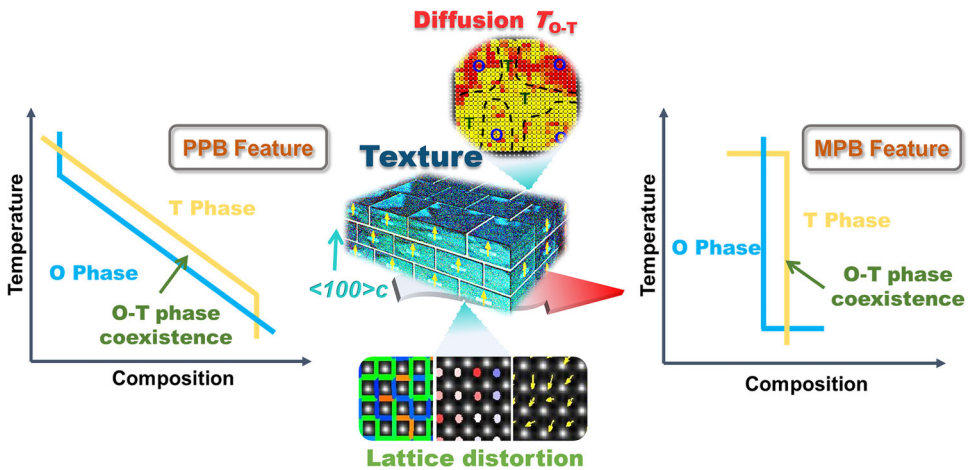

Fig. 1 | Schematic diagram. The strategy of achieving temperature stability in KNN-based ceramics through mimicking PZT's MPB structure.

https://doi.org/10.1038/s41467-024-53437-5

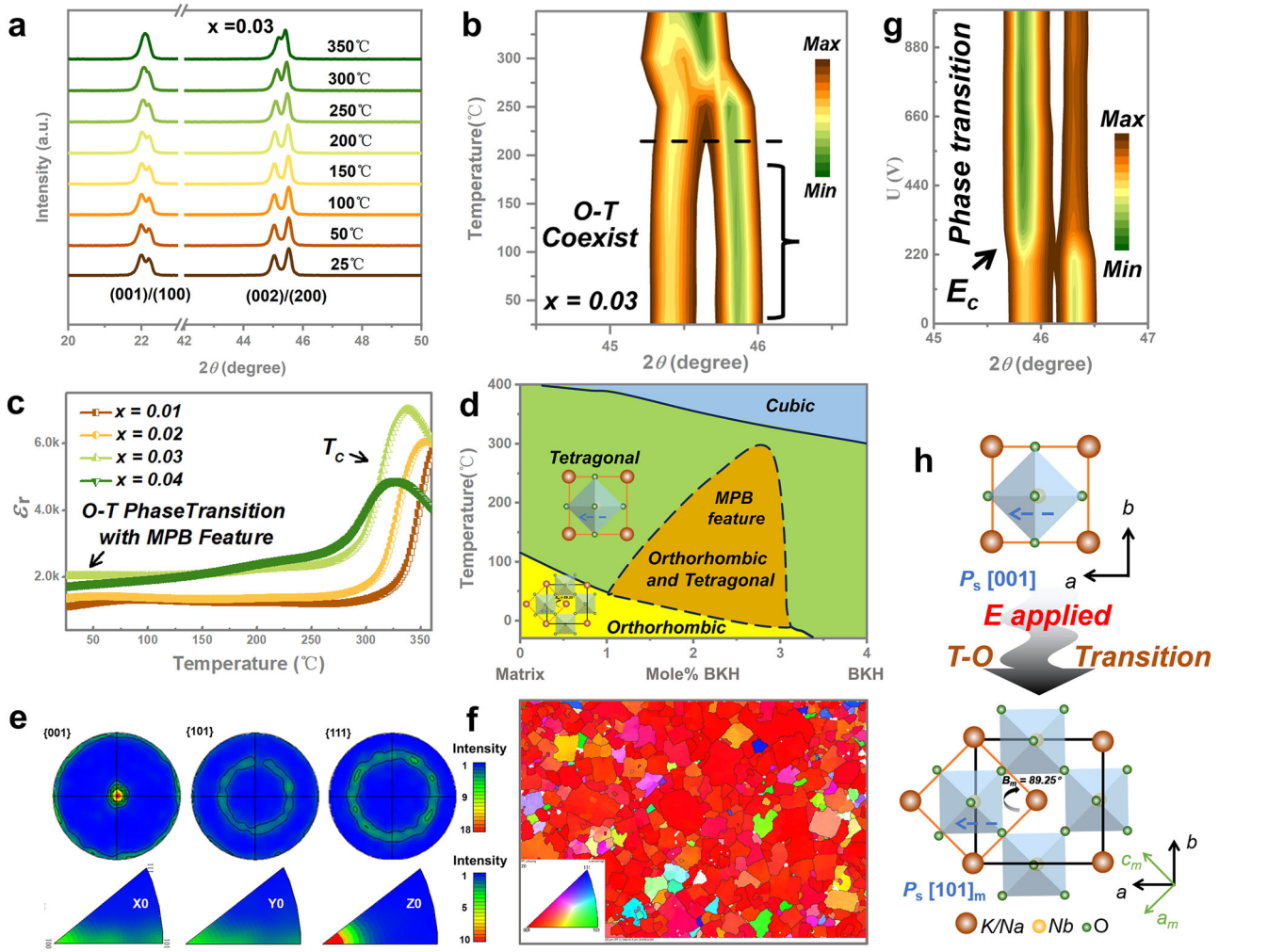

Fig. 2 | The analysis of crystal orientation and phase structure. a, **b** In-situ variable temperature XRD of 3T ceramics. **c** Temperature-dependent dielectric constant (ε_r-T) curves of xT ceramics. **d** Phase diagrams of xT ceramics. **e** EBSD pole diagram testing along the direction perpendicular to the casting direction of 3T ceramics. **f** EBSD inverse pole diagram testing along the direction perpendicular to the casting direction of 3T ceramics. **g** In-situ variable electric fields XRD for the 3T ceramics. **h** Schematic diagram of crystal structures for O phase-Amm2, T phase-P4mm, and T-O sequential phase transition.

impurity phases, as shown in Fig. S3. The X-ray diffraction (XRD) patterns of KNN-BNZ-xBKH ceramics for both random and textured ceramics are shown in Figs. S4a and S5. All samples exhibit typical perovskite structure and the (00l) diffraction peaks of the textured ceramics are significantly higher than those of the random ceramics, indicating strong crystal orientation along <00l>c. The Lotgering factor $f_{(00l)}$ can be used to calculate the texturing degree of the sample, and the corresponding $f_{(00l)}$ was calculated to be 98.7%, 98.3%, 98.7%, and 85.8% for the textured ceramics with $x = 0.01 - 0.04$, respectively[37]. In addition, the electron backscattered diffraction (EBSD) pole diagram (Fig. 2e) and inverse pole diagram (Fig. 2f) of 3T ceramics were tested along the direction perpendicular to the casting direction, indicating the high texture degree of the ceramics. The high orientation degree is attributed to the high-quality $NaNbO_3$ templates and reasonably designed sintering process. The phase structure with varied BKH concentration can be determined by combining the (002)/(200) characteristic diffraction peaks, ε_r-T curves, and Raman spectrum. As shown in Fig. S4a, with the increase of x, the intensity of the (002) peak in xR ceramics is gradually exceeded by (200), and even almost disappears, indicating that a continuous phase transition occurs, e.g., a gradual increase of the T phase and a gradual decrease of the O phase. In addition, as shown in Fig. S4b, with the increase of x, although the O-T phase boundary cannot be clearly seen, it gradually shifted to low temperature, while the R-O phase boundary was significantly suppressed and disappeared at liquid nitrogen temperature. Therefore, combining the analyses of both XRD patterns and ε_r-T curves, we can deduce that the 0R ceramics belong to the single orthogonal phase, while the xR ceramics with $0.01 \le x \le 0.04$ can be determined as the coexistence of O and T phases. Due to the presence of $T_{O\text{-}T}$ at room temperature, the 3R ceramics have a comparable content of O and T phases, which greatly reduces the Gibbs free energy and contributes to the improvement of ferro/piezoelectrical properties. On the contrary, due to the $T_{O\text{-}T}$ deviates from room temperature, 2R and 4R ceramics have more O and T phases, respectively. Hence, the room temperature ε_r of the xR ceramics first increases because it approached to the phase boundary (i.e., $x = 0 - 0.03$), but then decreases because of the reduced degree of phase boundary and the significantly destroyed long-range ordering at high contents of $(Bi_{0.5}K_{0.5})HfO_3$ (i.e., $x = 0.04$)[38].

It is noteworthy that the phase transition law of the xT ceramics is similar to that of the xR ceramics (Fig. S5), and the $T_{O\text{-}T}$ of 3T is also located at room temperature (Fig. 2c, Figs. S6 and S7). However, the O-T phase boundary of xT ceramics almost disappears, in particular $x = 0.03$, the phase structures exhibit similarities to the MPB structure in PZT (Fig. 2c). Thus, unlike other KNN-based ceramics, the corresponding phase diagrams represented by xT ceramics can be drafted as shown in Fig. 2d. KNN-based ceramics with MPB feature will

https://doi.org/10.1038/s41467-024-53437-5

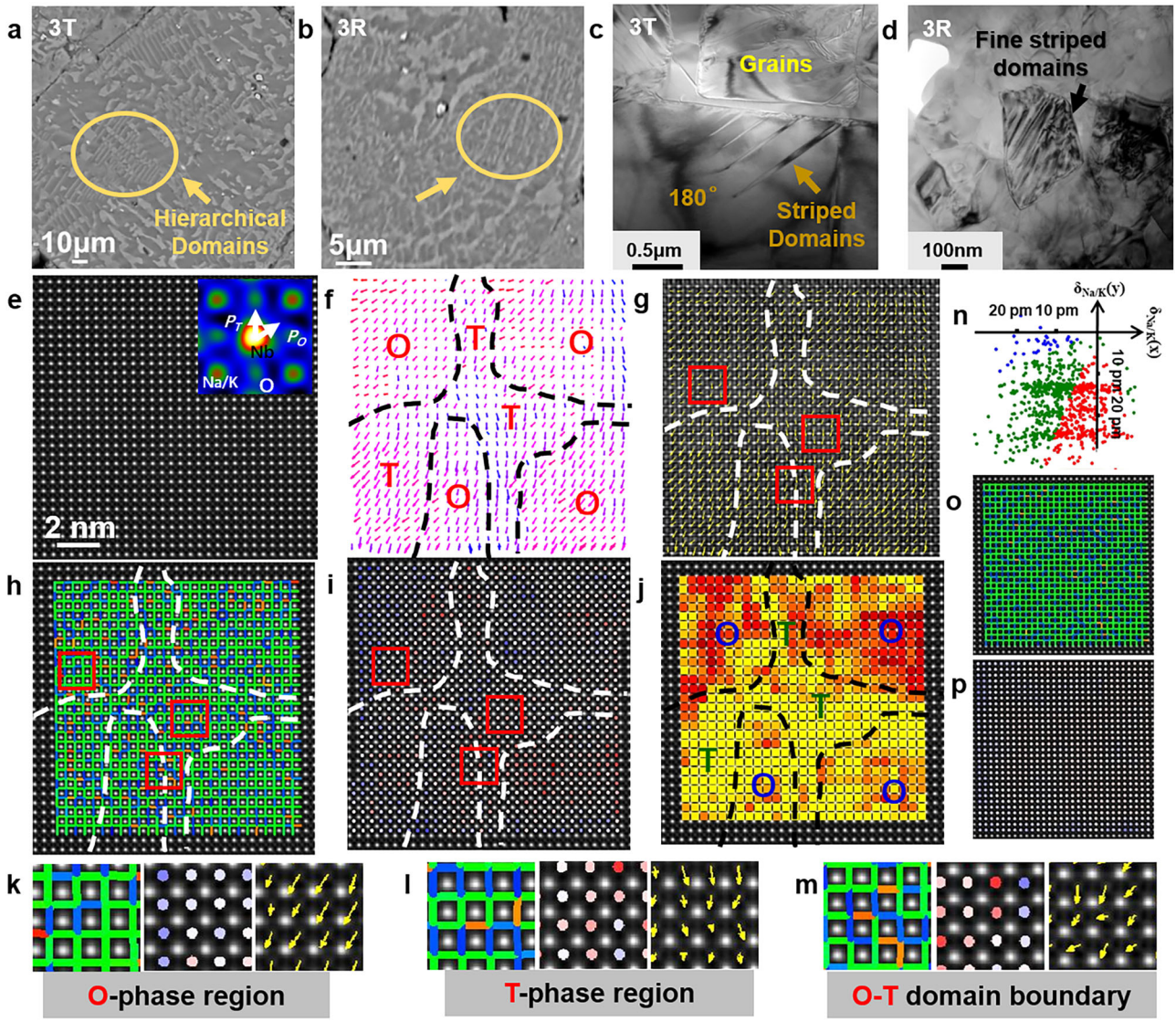

Fig. 3 | Domain structure and atomic local distortion. a SEM images for the 3T. **b** SEM images for 3R ceramics. **c** TEM images for the 3T ceramics. **d** TEM images for the 3R ceramics. **e** Atomically-resolved STEM HAADF image along [100], with an inset schematic projection of the ABO_3 unit cell along the [100] zone axis, marked polarization directions for T and O phases. **f** The $\delta_{Nb\text{-}O}$ displacement vector map and O and T regions are marked. **g** The contrast-reversed simultaneously acquired STEM ABF image superimposed with a map of atom polarization vectors. **h** Calculation of the key length of A sites. **i** Utilized the Z-contrast feature of STEM drawing the B-site intensity map. **j** Mapping of domain walls. **k**–**m** Enlarged images of local regions from the O phase, T phase, and the boundary of the O-T phase, extracted from (**h**–**j**) respectively. **n** Polarization direction histogram. **o** Calculation of the key length of B-site. **p** Utilized the Z-contrast feature of STEM drawing the B sites intensity map.

correspondingly exhibit excellent temperature stability of ferro/piezoelectrical properties. To further illustrate the newly discovered phase boundary of *x*T ceramics, the in-situ variable temperature XRD patterns are shown in Fig. 2a, b. From the measurements, not only the high Curie temperature of 3T ceramics can be observed (~330 °C), but the phase structure (coexistence of O and T phases) is also stable from room temperature to ~200 °C, revealing the phase boundary in 3T ceramics are similar to MPB, which is consistent with the ε_r-*T* curves. In addition, we also conducted XRD Rietveld refinement as shown in Fig. S8. The results indicate that there is a coexisting O-T phase structure in the temperature range of 25–200 °C, and the changes are very subtle with increasing temperature. At 25 °C, 100 °C, and 200 °C, the proportion of O phase is 68.378%, 65.206%, and 62.093%, respectively. Finally, the phase structure transforms to a cubic phase and a small amount of T phase at 350 °C. Overall, the multiphase coexistence phase boundary with MPB feature and high <00*l*> crystallographic orientation will play an important role in obtaining excellent comprehensive piezoelectricity for the 3T ceramics.

To further resolve the local structural information of the textured KNN-BNZ-BKH ceramics, aberration-corrected atomic-resolution scanning transmission electron microscopy (STEM) was employed. Fig. 3e gives a STEM annular Bright-Field (ABF) image along the [100] zone axis. For ferroelectric KNN-based materials, the polarization vectors are determined by the displacement from B-site cations (stronger intensity contrast, Nb) to the center of the four nearest neighboring A-site cations (weaker intensity contrast, Na/K) based on 2D Gaussian peak fitting. It is clearly shown that the $\delta_{Nb-Na/K}$ vectors are not homogeneous (as expected in normal ferroelectrics with a single phase); instead, they are heterogeneous, i.e., mainly lying along the pseudocubic axes in the left part and along the diagonals in the right part, corresponding to the T and O symmetries, respectively, as schematically shown in the inset of Fig. 3e. After peak finding with the method of 2D Gaussian peak fitting, with an accuracy ~5 pm, the $\delta_{Nb\text{-}O}$ displacement vector map can be obtained, as shown in Fig. 3f, g. Based on the schematic figure (the inset), T and O nanoregions can be identified, which is consistent with XRD analysis results. The

dominance of large-scale long-range ordered polarization regions consisting of O and T phases can be clearly observed by combining the arrows in the zone axis along [100] zone axis, while short-range disordered multiphase nanoclusters occupy less, which is quite different from the local structure of KNN-based ceramics with R-O-T multiphase coexistence[9,17]. Fig. 3n is a statistical chart of the polarization direction in quadrants. The results indicate that the O phase is the majority phase. Fig. 3f, g clearly shows the gradual polarization rotation between different states. Such nanoscale balanced multiphase coexistence may possess almost isotropic free energy and thus significantly decreased polarization anisotropy.

We also performed the calculation of the key length of both A and B sites, as shown in Fig. 3h, o, the reddish lines indicate longer bond lengths, the bluish lines indicate shorter bond lengths, and the green lines represent the average normal bond lengths. We utilized the Z-contrast feature of STEM to draw the A site intensity map, as shown in Fig. 3i, p, the reddish atoms represent heavier elements, while the bluish atoms indicate lighter elements. Fig. 3k–m present the local images of the O phase, T phase, and the boundary of the O-T phase, respectively, extracted from Fig. 3h–j. It can be observed that the O regions exhibit less heavy dopants (Bi) in A sites and weaker lattice distortion, compared with the T regions; while the O-T phase boundary regions show the most dopants and strongest lattice distortion. The local segregation of doping elements leads to the formation of the phase coexistence of O and T nanophases. As shown in Fig. 3o, p, the bond lengths and the atom intensities at B sites are relatively uniform, with fewer fluctuations, which is due to the relative differences in the atom size and atom number between B-site dopants (Zr and Hf) and Nb matrix are relatively small, compared with the A-site dopants Bi and K/Na matrix (Tables S1 and S2). The results provide insights into the relationship between A/B-site doping and the formation of the O-T phase boundary, guiding the doping behavior of KNN-based piezoelectric ceramics.

Ferroelectricity and piezoelectricity

Fig. S9a demonstrates the *P-E* hysteresis loops of the *x*T ceramics tested at 30 kV/cm and 10 Hz. Although the coercive field ($\mathbf{E}_c$) of *x*T ceramics is comparable to that of *x*R ceramics, all the *x*T ceramics exhibit more well-saturated square *P-E* hysteresis loops with relatively larger remnant polarization ($\mathbf{P}_r$) and maximum polarization ($\mathbf{P}_{max}$) than *x*R ceramics (Fig. S9b), such as, the $\mathbf{P}_r$ is close to 28 μC/cm^2 in 3T ceramics, while in 3R ceramics, the $\mathbf{P}_r$ is only around 21 μC/cm^2, indicating enhanced ferroelectricity. The crystal orientation makes the arrangement of dipoles more effective under the applied electric field, thereby improving the polarization efficiency and ferroelectricity of *x*T ceramics. The ferroelectricity is also influenced by the phase structure. It can be seen that the changes in $\mathbf{P}_r$ and $\mathbf{P}_{max}$ of the KNN-BNZ-*x*BKH ceramics regardless of texture and random keep increasing from $x = 0.01$ to 0.03 as the O-T phase boundary gradually moved towards room temperature, and then decrease at $x = 0.04$. Meanwhile, $\mathbf{E}_c$ also gradually decreases with the increase of the T phase, consistent with previously reported results[39]. This is initially associated with a decrease in free energy due to the emergence of the phase boundary, followed by an increase in relaxor feature due to the gradual dominance of the T phase. Compared with their random counterparts, the textured ceramics achieved significant improvements in both strain and piezoelectricity, especially for the 3T ceramics, which not only possessed both high piezoelectric coefficient and high Curie temperature (d_{33}~550 pC/N, T_C~330 °C, Fig. S10b), but also observed a large strain of ~0.2% at 30 kV/cm (Fig. S10a). Such excellent comprehensive performance is highly competitive in lead-free piezoceramics (Fig. S11)[3,5,9,25,27,34,35,40–47]. It should be noted that the random and textured KNN-BNZ-*x*BKH ceramics share a similar chemical composition and room temperature phase structure, and the significant difference in piezoelectricity between them mainly stems from the high crystal orientation. Therefore, the superposition of the effective arrangement of dipoles caused by the preferred crystal orientation and the low domain wall energy of the phase boundary contributes to the easy polarization rotation along different polarization states under an external electric field, thus obtaining a high piezoelectric response.

To further establish the relationship between performance and microstructure, the 3T ceramics were subjected to in-situ electric field X-ray diffraction tests, and the corresponding (200)/(002) peaks are shown in Fig. 2g and Fig. S12. As the applied electric field increases, the position of (002)/(200) peaks slightly moved to the lower 2θ due to the lattice distortion caused by electric field. More importantly, it is also observed that the peak intensity ratios of the (002)/(200) change gradually with the increase of the applied electric field, resulting in a continuous phase transition from the O-T phase to the pure O phase, in particular near the coercive field (~14 kV/cm). Fig. 2h shows the crystal structure evolution of the T-O sequential phase transition. The above results provide key evidence to reveal that efficient polarization rotation occurs inside the 3T ceramics under the action of an external electric field[18]. It is noteworthy that the phase transition is almost irreversible after the withdrawal of the electric field, indicating a high irreversible lattice distortion, leading to high residual polarization and excellent piezoelectricity.

The structure of domains is closely related to the electrical properties of ferroelectric materials[48–50], and the SEM images of acid-etched domain patterns are shown in Fig. 3a, b. Not only the morphology of the watermark domain, the T/O phase-related abundant hierarchical domain structure inside can be seen visually. The hierarchical domain architecture originates from low domain wall energy and almost disappeared polarization anisotropy, typically occurring in multiphase coexisting regions, which not only facilitates the reduction of the coercive field but also plays an important role in the construction of diffusion-type phase boundary[29]. In addition, it can be seen from the complete SEM images that there is a significant difference in the grain size between 3R ceramics and 3T ceramics, as shown in Fig. S13. Due to the large grain size, the overall domain size in 3T ceramics is significantly larger than that in 3R ceramics, which can be further verified in TEM images (Fig. 3c, d, and Fig. S14). The reduced coercive field caused by fewer grain boundaries and the preferred crystal orientation compensates for the increased domain wall energy of the larger domains, resulting in comparable $\mathbf{E}_c$ in *x*T and *x*R ceramics (Fig. S9a, b), which allows the larger-sized domains in 3T ceramics to undergo efficient switching and contributes to a more saturated polarization. Therefore, the high piezoelectric response of 3T ceramics also benefits from the contribution of larger-size domains. In addition, from the element mapping images of TEM, it can be further clearly seen that the several main elements in 3T ceramics are uniformly distributed without obvious impurities (Fig. S15).

Piezoelectric temperature stability

The heat generated by piezoelectric materials during service or fluctuations in external temperature can cause changes in the temperature of the material itself. Therefore, in addition to focusing on the performance of piezoelectric materials at room temperature, the temperature stability of piezoelectric performance is also a very important indicator for transducer and sensor applications, especially the small signal piezoelectric coefficient d_{33} (i.e., direct piezoelectric effect)[51–54]. It is well known that d_{33} is proportional to $\varepsilon_r \cdot \mathbf{P}_r$, so the temperature stability of both dielectric constant and ferroelectricity are closely related to the piezoelectric temperature insensitivity. As shown in the ε_r-*T* curves (Fig. 2c), it can be seen that the O-T phases boundary with MPB feature makes the ε_r of 3T ceramics rise slowly between room temperature and Curie temperature, and remains almost at a horizontal line until 150 °C. In contrast, from the in-situ variable temperature *P-E* hysteresis loops (Fig. S16), it can be found that both the $\mathbf{P}_{max}$ and $\mathbf{P}_r$ decrease slowly from room temperature to 180 °C. Thus, the complementary effect between

https://doi.org/10.1038/s41467-024-53437-5

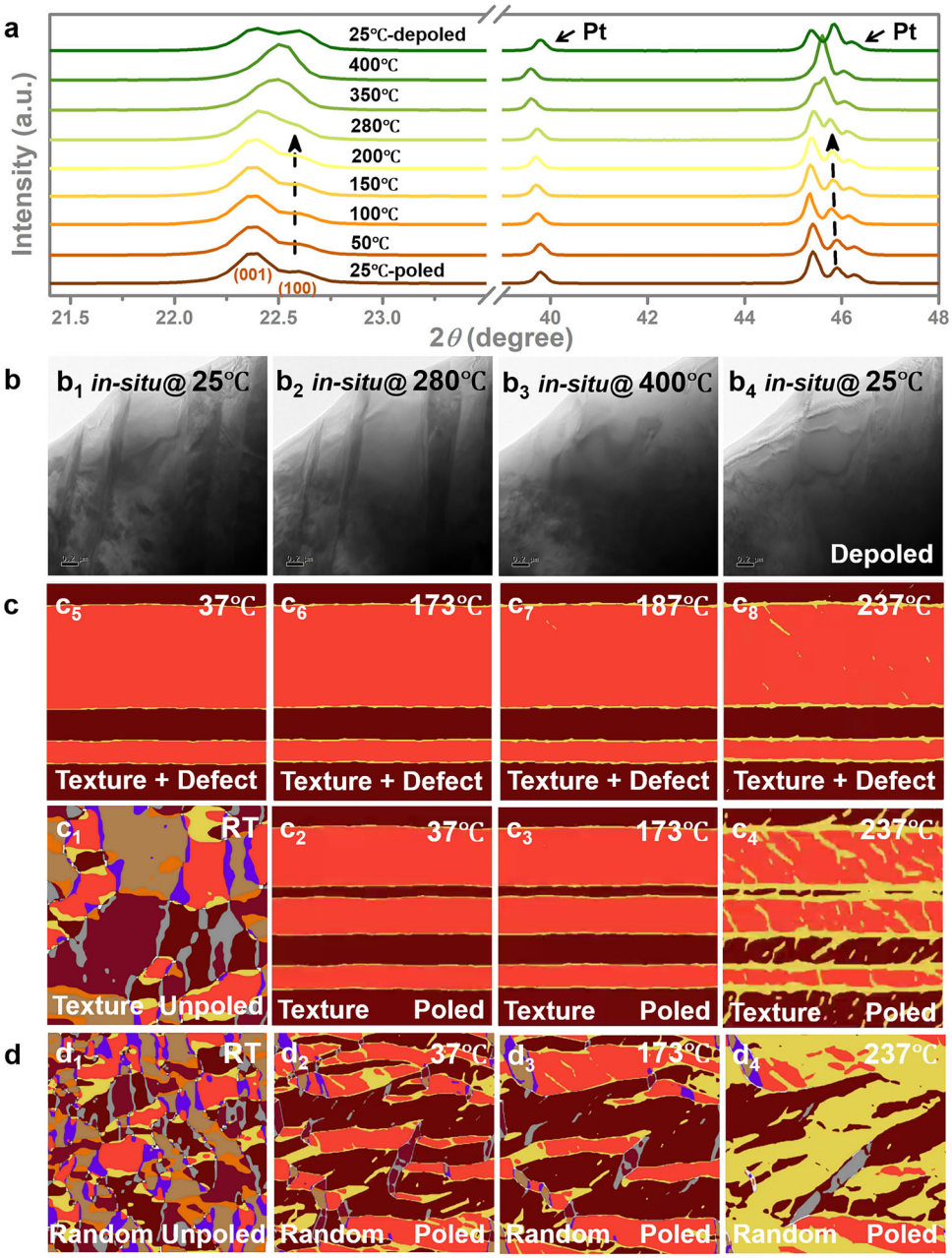

Fig. 4 | Temperature-induced phase structure and domain structure evolution. **a** In-situ variable temperature XRD for the 3T ceramics after poled. **b** In-situ variable temperature TEM images for the 3T ceramics after poled (b_1–b_4). **c** Phase-field simulation results of room temperature domain structure images for textured ceramics before poled (c_1), variable temperature domain structures images for textured ceramic after poled (c_2–c_4), and variable temperature domain structures images for textured ceramics with defect pinning after poled (c_5–c_8). **d** Phase-field simulation results of room temperature domain structure images for random ceramics before poled (d_1) and variable temperature domain structure images for random ceramics after poled (d_2–d_4).

the dielectric constant and $\mathbf{P}_r$ may lead to the temperature stability of the piezoelectricity for the 3T ceramics. The stability of piezoelectric performance is also closely related to the internal structure of ceramics, so we conducted a detailed analysis of the poled phase structure and domain structure. Fig. 4a shows the in-situ temperature-dependent XRD of 3T ceramics after poled. As the temperature increases, the XRD diffraction peaks remain basically unchanged below 200 °C. Peak fitting was performed on the (002)/(200) peaks (Fig. S17) in order to more accurately understand the changes in phase composition. As can be seen in Fig. S17b, only the single O phase exists in the range from room temperature to 150 °C, and the T phase begins to gradually emerge only when the temperature approaches 200 °C, exhibiting excellent temperature stability of the phase structure similar to that of the pre-poled one, which greatly improves the temperature stability of $\mathbf{P}_r$ and the post-poled ε_r.

Moreover, we also investigated the evolution of poled domain structure through in-situ variable temperature PFM and TEM measurements. It can be seen that after poled, the micron-scale macrodomains of the 3T ceramics (Fig. S18d) undergo efficient switching and domain growth, resulting in the phase of all domains becoming almost 180° (Fig. S18a), consistent with the high $\mathbf{P}_r$. Macroscopically, no significant large-scale poled domain recovery occurred when the temperature increases to 200 °C (Fig. S18a–c), which is another key factor for $\mathbf{P}_r$ to maintain good temperature stability. While locally, due to thermally stimulated degradation of some unstable smaller domain structures, the peak intensity of the ±180° domains gradually weakened with increasing

temperature (inset of Fig. S18a–c). The in-situ variable temperature TEM was further used to investigate the evolution of poled large-sized stripe domains with temperature in 3T ceramics, as shown in Fig. 4b. It can be clearly observed that the large-sized stripe domains can be well maintained at 280 °C. The number of domains has not decreased, and their morphology remains intact. When approaching the T_C, the corresponding domain structure begins to be destroyed and disappears, resulting in depolarization. In addition to stable phase structure, the large-sized domain structure plays an important role in resisting thermal depoled, as the disturbance of larger domain requires a higher driving force. To investigate the temperature response of internal structure for textured ceramics and random multiphase ceramics with different domain sizes after poled, phase-field simulation was employed. Several effects were considered in our model: Firstly, the ferroelectric polycrystal structures with different grain sizes (KNN system) were generated, resulting in textured or random orientations at different grains. Secondly, the random fields were employed due to the presence of defects caused by doping. After the domain structure evolution is stable, a polarization electric field of up to 3 kV/mm was applied to observe the changes in domain structure with temperature. Fig. 4c_1–c_4 and d show the simulated domain structure changes of the large macrodomains for the textured multiphase ceramics and the small macrodomains for the random multiphase ceramics after poled and the corresponding temperature response. The textured ceramics with larger domain structures exhibit a more saturated polarization state after poled, which is beneficial for piezoelectricity. More importantly, its poled domain structure can remain stable at higher temperatures without being damaged (e.g., >173 °C), which is consistent with actual experimental results. Furthermore, we also found through EPR tests that in addition to more oxygen vacancy defects introduced by the increase in *x*BKH, the oxygen vacancy content of *x*T ceramics was also higher than that of *x*R ceramics (Fig. S19). The generation of oxygen vacancies tends to form defect dipoles in ferroelectric ceramics and will be aligned along the applied electric field, which has a pinning effect on the poled domain structure and increases the depolarization energy, thus improving the domain stability[31], as shown in Fig. 4c_5–c_8. Therefore, comprehensive structural analysis and simulations have ascertained that in addition to the stable phase structure induced by the multiphase coexistence phase boundary with the MPB feature, the larger domain size and the pinning of defects are closely related to the temperature stability of the domain structure. The stability of phase and domain structures will be beneficial for the piezoelectric temperature stability.

Fig. 5a presents the in-situ temperature-dependent d_{33} of the *x*T ceramics ($x = 0.01 - 0.04$). Typically, when a PPT-type O-T phase boundary exists above room temperature, the d_{33} of KNN-based ceramics will shake up at $T_{O\text{-}T}$ and then drop with increasing temperature, showing extreme sensitivity to temperature[35]. Whereas, in *x*T ceramics, the temperature sensitivity of the piezoelectric coefficient d_{33} decreases as the diffusion of the O-T phase boundary increases with composition. For example, when $0.01 \le x \le 0.02$, the O-T phase boundaries are already very diffuse, effectively improving the temperature stability, which can be confirmed by the in-situ temperature-dependent d_{33} value of *x*R and *x*T in Fig. 5a, b. When the $T_{O\text{-}T}$ is further shifted to room temperature or even below room temperature, the phase boundary characteristics are even close to the MPB structure. Thus, for 3T ceramics, its high d_{33} remains almost unchanged (fluctuating by only 1.2%) from room temperature to 150 °C. Even in the range of 25–250 °C, its d_{33} decreases by only 10%, and significant changes occur only when T_C is reached. In random-oriented ceramics, the corresponding components ceramics are of poor temperature stability due to insufficient diffusion, as shown in Fig. 5b. Therefore, the new phase boundary with MPB feature obtains an unprecedented break through in temperature stability for high piezoelectric coefficient KNN-based ceramics (e.g., $d_{33} > 400$ pC/N) and also highly competitive concerning other studied Pb/Pb-free ceramics (Fig. 5c–e)[25,27,31,55–58]. The collaborative optimization of crystal orientation and design of new phase boundary involved in this work provides an important advance for optimizing the comprehensive piezoelectricity of KNN-based ceramics, especially temperature stability.

In summary, ultra-high temperature stability and piezoelectric coefficient were achieved in the 3T ceramics. Both the T/O phase local distortion associated with the O-T phase boundary in the atomic scale and the correlation between A/B-site doping and the formation of the O-T phase boundary can be confirmed by STEM. While XRD as well as EBSD can further resolve the macro-scale crystal orientation. Benefiting from the O-T multiphase coexistence at room temperature and high orientation, the material undergoes irreversible electric field-induced efficient large-size macro-domain switching and phase transitions, which exhibit high residual polarization as well as a significantly improved d_{33}. In addition, the synergistic effect between the ultra-high stability of phase structures and domain structures through mimicking PZT's MPB structure is the reason why the 3T ceramics break through the inherent drawbacks of temperature instability. The intrinsic reason is related to the induction of larger-size hierarchical domain structure and the formation of point defect during the grain template growth method (TGG), which greatly improves the depolarization energy of the KNN-BNZ-*x*BKH textured ceramics. Finally, the excellent thermal stability, with a change rate of less than 1.2% in the temperature range of 25–150 °C and less than 10% in the temperature range of 25–250 °C, coupled with high piezoelectric coefficient (d_{33}) ~550 pC/N and high Curie temperature (T_C)~330 °C, making the 3T ceramics a promising candidate for future lead-free piezoelectric ceramics applications.

Methods

Sample preparation

The $(0.97\text{-}x)(Na_{0.56}K_{0.44})NbO_3$–$0.03Bi_{0.5}Na_{0.5}ZrO_3$-$x(Bi_{0.5}K_{0.5})HfO_3$ (KNN-BNZ-*x*BKH) ($0.01 \le x \le 0.04$) lead-free random and textured piezoceramics were designed and prepared using conventional solid-state method and template grain growth (TGG) method, respectively. All raw materials, including Na_2CO_3 (Aladdin, 99.8%), K_2CO_3 (Aladdin, 99.99%), Nb_2O_5 (Aladdin, 99.98%), Bi_2O_3 (Alpha, 99.98%), ZrO_2 (Aladdin, 99.99%) and HfO_2 (Alpha, 99.99%) were ball milled with ethyl alcohol and ZrO_2 balls after weighting according to the formula. The milled powders were calcined at 840–850 °C for 5 h after the ethyl alcohol dried off, then ball milled again for 12 h and dried.

Random piezoceramics

The KNN-BNZ-*x*BKH matrix powders pressed into disks of 12-mm diameter and 1-mm thickness under the pressure of 200–300 MPa with a binder of 6 wt% polyvinyl alcohol. Subsequently, the pellets were heated to 600 °C at 1 °C/min to burn out the binder and then sintered at the target temperature by two-step sintering, which was heated to 1150–1170 °C and then rapidly cooled to 1050–1070 °C for 10 h. In addition, the traditional one-step sintering involved in this work was to heat to the target temperature at a speed of 3 °C/min, and then conduct heat preservation and furnace cooling.

Textured piezoceramics

To prepare tape-casting slurries, the KNN-BNZ-*x*BKH matrix powders, 4 mol % $NaNbO_3$ templates, and organic binders were mixed in a solvent (50 wt% alcohol and 50 wt% toluene). Then, the slurries with good liquidity were casted and form green tapes. The dried tapes were stacked and then pressed to form dense green bodies, which were pressed into disks of 12 mm × 12 mm and 1 mm thickness under the pressure of 200–300 MPa. Subsequently, the pellets were heated to 600 °C at 1 °C/min to burn out the binder and then sintered at the target temperature by two-step sintering, which was heated to 1180–1220 °C and then rapidly cooled to 1080–1120 °C for 10 h.

https://doi.org/10.1038/s41467-024-53437-5

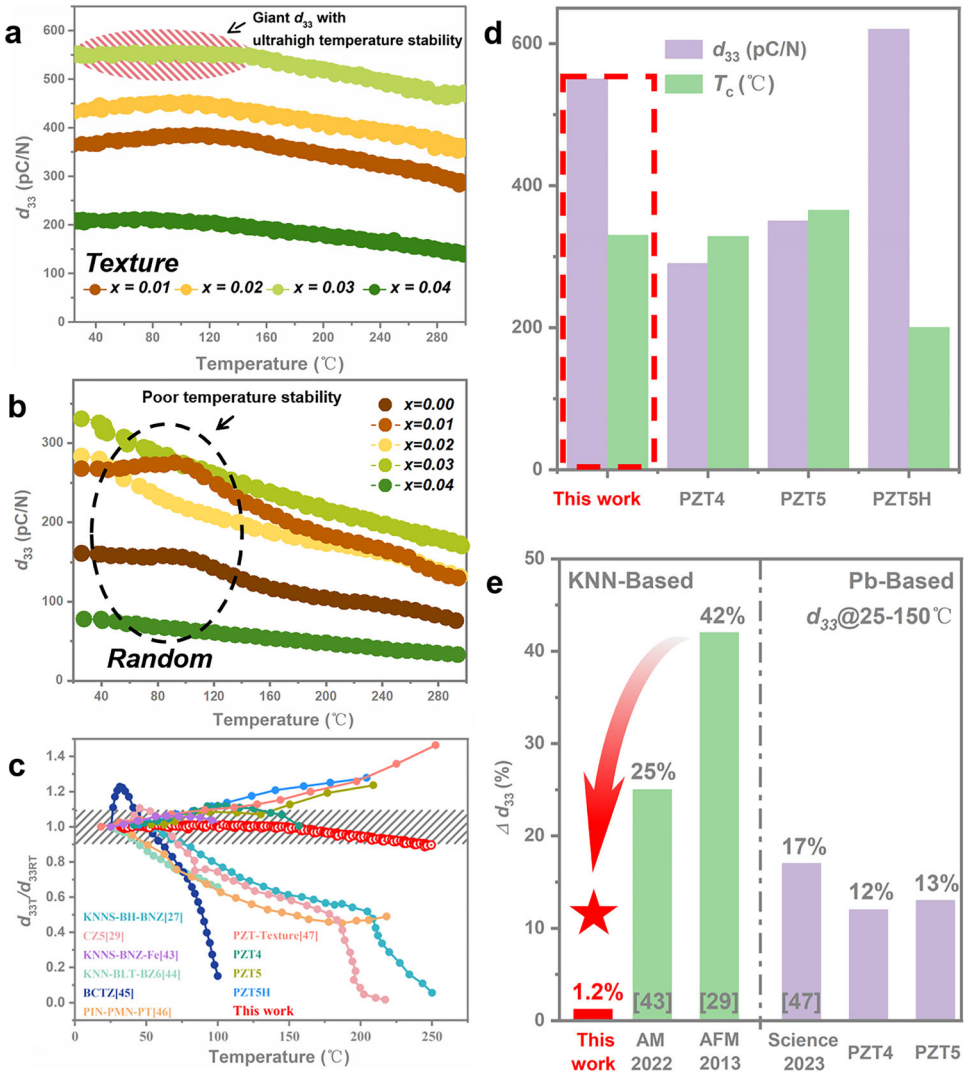

Fig. 5 | Temperature stability of piezoelectricity. a In-situ temperature-dependent d_{33} value of the xT ceramics. **b** In-situ temperature-dependent d_{33} value of the xR ceramics. **c** Comparison of the temperature-dependent in-situ d_{33} variation curves of 3T ceramics in this work with other ceramics reported in the literature. **d** Comparison of d_{33} and T_c of the 3T ceramics in this work with PZT-based ceramics reported in the literature. **e** Comparison of temperature-dependent in-situ d_{33} change rate of the 3T ceramics in this work with other ceramics reported in the literature.

Characterization of electrical properties

Via mechanically thinning to 0.5 mm thickness, xT, and xR ceramics were coated by Ag electrodes on both sides for dielectric, ferroelectric, and electric field-induced strain tests. Polarization (*P*-*E*) and strain (*S*-*E*) hysteresis loops were measured using a ferroelectric test system (Precision Premier II) at 10 Hz. The temperature-dependent polarization (*P*-*E*) loops were achieved by the ferroelectric test system (Precision Premier II) with a heating stage. After poled at 30 kV cm^{-1} by AC electric field at room temperature, the piezoelectric coefficient (d_{33}) was tested at room temperature using a quasi-static d_{33} meter (ZJ-6A, Institute of Acoustics, China). The temperature-dependent piezoelectric coefficient (d_{33}) was tested by a quasi-static d_{33} meter (YE2730A, Sinocera, China), which was connected to a heating furnace. The temperature-dependent dielectric constants (ε_r-T) curves were achieved by the Agilent E4980A LCR meter and the Keithley 2410 Source Meter equipped with a heating stage (−110 to 400 °C).

Structural characterization

The surface and cross-section microstructure of the ceramics were investigated with a scanning electron microscope (SEM, HITACHI, TM4000Plus). Electron backscatter diffraction (EBSD) pole figure and inverse pole figure for texture degree analyses and energy-dispersive X-ray spectroscopy (EDS) were obtained by a field emission scanning electron microscope (FEI Magellan 400). The room temperature phase structure of the ceramics was tested using an X-ray diffractometer (XRD, Bruker D2 PHASER). The specimens for transmission electron microscopy (TEM) were prepared by mechanical thinning, ultrasonic cutting, and Ar-ion thinning until electrons can penetrate the samples with a thickness of ~30–50 nm. A JEOL JEM-2100F microscope was used to acquire the bright-field images for domain morphology. Oxygen vacancy defects were proved by EPR (Bruker A300). Acid-etched domain structures were observed on a scanning electron microscopy (SEM) JSM-7610F. Before acid-etching, preparatory work such as lapping and polishing was performed at room temperature. A mixed aqueous solution of HCl acid (with the mass concentration of about 37%, Laiyang Kangde Chem. Co., Ltd.) and HF acid (with a mass concentration ≥40%, Tianjin Kemiou Chemical Reagent Co., Ltd.) in a volume ratio of 1:1 was used the etchant. The specimens for transmission electron microscopy (TEM) and atomic-resolution scanning transmission electron microscopy (STEM) were prepared by mechanical thinning, ultrasonic cutting, and Ar-ion thinning until electrons can penetrate the samples with a thickness of ~30–50 nm. To reduce the

impact of temperature on the poled sample, not only the required hot melt adhesive operation temperature for mechanical thinning is controlled at around 100 °C or as low as possible, but also liquid nitrogen is assisted in the Ar-ion thinning process. A JEOL JEM-2100F microscope was used to acquire the bright-field images for domain morphology. The atomic-scale imaging was carried out on a Cs-corrected Hitachi HF5000 microscope with ultra-high resolution (UHR) mode and a convergence/collection semi-angle of 20 mrad/60–320 mrad.

In-situ structural characterization

In-situ XRD under different temperatures was collected using X-ray diffractometer (PANalytical Empyrean, Holland). One self-made in-situ electric field XRD sample holder was used to test the phase structure at different applied voltages (0–1000 V, sample thickness ~0.3 mm). The translucent gold electrodes by DC sputtering are used as electrodes for testing the in-situ variable electric field XRD. In-situ Raman spectra were obtained at different temperatures using a Horiba Lab-Ram HR800 spectrometer with a laser wavelength of 532 nm accompanied by an additional temperature probing stage. In-situ optimized vertical piezoresponse force microscopy (OV-PFM) images under different temperatures were obtained by piezoresponse force microscope with additional temperature probing stage (PFM, Dimension Icon, Bruker, United States). The temperature-induced domain evolution was observed by a transmission electron microscope (TEM, JEM 2100 F) equipped with a heating stage.

Phase-field model

To describe the domain structures in textured and random grain structures, an order parameter η was employed to represent the different crystal orientations. To separate the different grain orientations, two sets of coordinate system was used. The domain structures within each grain can be described as local spontaneous polarization $\mathbf{P}_L$. In the global coordinate system, a global polarization $\mathbf{P}$ and a displacement field $\mathbf{u}$ were adopted as the order parameters in the phase-field model. The temporal evolution of the polarization is described by the time-dependent Ginzburg-Landau (TDGL) equation and the stress/electric field equilibrium equation[59],

$$\frac{\partial \mathbf{P}_i}{\partial t} = -L\frac{\delta F}{\delta \mathbf{P}_i} + \mathbf{E}_i^{thermal} \tag{1}$$

$$\frac{\partial}{\partial x_j}(\sigma_{ij}(r,t)) = 0 \tag{2}$$

$$\mathbf{D} = \rho_f \tag{3}$$

Here, L is a kinetic coefficient related to domain wall mobility, F is the total free energy of the system, $\frac{\delta F}{\delta \mathbf{P}_i}$ is the thermodynamic driving force, σ_{ij} is the stress tensor, $\mathbf{D}$ is the electric displacement, ρ_f is the free charge density, r, and t are the spatial coordinate and time, respectively. The total free energy of a bulk system can be defined as follows,

$$\begin{aligned} F &= F_{Land}(\mathbf{P}) + F_{grad}(\mathbf{P}) + F_{elastic}(\mathbf{P}) + F_{elec}(\mathbf{P},\mathbf{E}) \\ &= \int_V (f_{Land} + f_{grad} + f_{elastic} + f_{elec})dV \end{aligned} \tag{4}$$

Where F includes the bulk free energy $F_{bulk}(\mathbf{P})$, domain wall energy $F_{grad}(\mathbf{P})$, elastic energy $F_{elastic}(\mathbf{P})$, and electrostatic energy $F_{elec}(\mathbf{P},\mathbf{E})$, $\mathbf{E}$ is the applied static electric field. f_{Land}, f_{grad}, f_{elastic} and f_{elec} are the corresponding energy density.

The bulk free energy density in a given grain can be expanded in terms of polarization components. For the KNN system, the bulk free energy density can be described as:

$$\begin{aligned} f_{Land} = {} & a_1\left(\mathbf{P}_{L1}^2 + \mathbf{P}_{L2}^2 + \mathbf{P}_{L3}^2\right) + a_{11}\left(\mathbf{P}_{L1}^4 + \mathbf{P}_{L2}^4 + \mathbf{P}_{L3}^4\right) \\ & + a_{12}\left(\mathbf{P}_{L1}^2\mathbf{P}_{L2}^2 + \mathbf{P}_{L1}^2\mathbf{P}_{L3}^2 + \mathbf{P}_{L2}^2\mathbf{P}_{L3}^2\right) + a_{11}\left(\mathbf{P}_{L1}^6 + \mathbf{P}_{L2}^6 + \mathbf{P}_{L3}^6\right) \\ & + a_{112}\left[\mathbf{P}_{L1}^4\left(\mathbf{P}_{L2}^2 + \mathbf{P}_{L3}^2\right) + \mathbf{P}_{L3}^4\left(\mathbf{P}_{L2}^2 + \mathbf{P}_{L1}^2\right) + \mathrm{P}_{L2}^4\left(\mathbf{P}_{L3}^2 + \mathbf{P}_{L1}^2\right)\right] \\ & + a_{123}\mathbf{P}_{L1}^2\mathbf{P}_{L2}^2\mathbf{P}_{L3}^2 + a_{1111}\left(\mathbf{P}_{L1}^8 + \mathbf{P}_{L2}^8 + \mathbf{P}_{L3}^8\right) \\ & + a_{1112}\left[\mathbf{P}_{L1}^6\left(\mathbf{P}_{L2}^2 + \mathbf{P}_{L3}^2\right) + \mathbf{P}_{L3}^6\left(\mathbf{P}_{L2}^2 + \mathbf{P}_{L1}^2\right) + \mathbf{P}_{L2}^6\left(\mathbf{P}_{L3}^2 + \mathrm{P}_{L1}^2\right)\right] \\ & + a_{1122}\left(\mathbf{P}_{L1}^4\mathbf{P}_{L2}^4 + \mathbf{P}_{L1}^4\mathbf{P}_{L3}^4 + \mathbf{P}_{L2}^4\mathbf{P}_{L3}^4\right) + a_{1123}(\mathbf{P}_{L1}^4\mathbf{P}_{L2}^2\mathbf{P}_{L3}^2 + \mathbf{P}_{L1}^2\mathbf{P}_{L2}^4\mathbf{P}_{L3}^2 \\ & + \mathbf{P}_{L1}^2\mathbf{P}_{L2}^2\mathrm{P}_{L3}^4) \end{aligned} \tag{5}$$

where G is the Gibbs free energy of a cubic ferroelectric system, $a_1 - a_{1123}$ is the Landau coefficient and $\mathbf{P}_L$ is the polarization field in the local crystallographic coordinate system within each grain. A standard global coordinate system for all grains was introduced to solve the polycrystal's elasticity and electrostatic equilibrium equation. Three Euler angles were used to describe the orientation of different grains in the polycrystalline structure. Thus, the transformation matrix from the global to local coordinate system is given by:

$$tr = \begin{Bmatrix} \cos\varphi\cos\psi - \cos\theta\sin\varphi & \sin\psi\sin\varphi\cos\psi + \cos\theta\cos\varphi\sin\psi & \sin\theta\sin\psi \\ -\cos\theta\cos\psi\sin\varphi - \cos\varphi\sin\psi & \cos\theta\cos\varphi\cos\psi - \sin\varphi\sin\psi & \sin\theta\cos\psi \\ \sin\theta\sin\varphi & -\cos\varphi\sin\theta & \cos\theta \end{Bmatrix} \tag{6}$$

The polarization in the local coordinate system can be described as a transformation from the polarization in the global coordinate system through

$$\mathbf{P}_{Li} = \frac{1}{2}tr_{ij}\mathbf{P}_j \tag{7}$$

The gradient energy density in an anisotropic system can be calculated by

$$f_{grad} = \frac{1}{2}g_{ijkl}\mathbf{P}_{i,j}\mathbf{P}_{k,l} \tag{8}$$

where g_{ijkl} is the gradient energy coefficient and $\mathbf{P}_{i,j} = \frac{\partial \mathbf{P}_i}{\partial x_j}$. The elastic energy density can be described as:

$$f_{elas} = \frac{1}{2}c_{ijkl}e_{ij}e_{kl} = \frac{1}{2}c_{ijkl}(\varepsilon_{ij} - \varepsilon_{ij}^0)(\varepsilon_{kl} - \varepsilon_{kl}^0) \tag{9}$$

where c_{ijkl} is the stiffness tensor, e_{ij} is the elastic strain tensor, ε_{ij} is the total strain tensor, and is the eigenstrain,

$$\varepsilon_{ij}^0 = \varepsilon_{Lij}^0 = Q_{ijkl}\mathbf{P}_{Lk}\mathbf{P}_{Ll} \tag{10}$$

Where ε_{Lij}^0 is the eigenstrain with respect to the local coordinate system, Q_{ijkl} is the electrostrictive coefficient tensor. Therefore, the eigenstrain in the global coordinate system can be obtained from

$$\varepsilon_{ij}^0 = tr_{ki}tr_{lj}\varepsilon_{Lkl}^0 \tag{11}$$

The electrostatic energy density f_{elec} of the system in phase-field simulation is given by,

$$f_{elec} = -\mathbf{P}_i(r)(\mathbf{E}_i(r) + \mathbf{E}_{RF}) - \frac{1}{2}\mathbf{P}_i(r)\mathbf{E}_i^{in}(r) \tag{12}$$

where $\mathbf{E}_i^{in}(r)$ is the E-field induced by the dipole moments, $\mathbf{E}_i(r)$ is the applied electric field and $\mathbf{E}_{RF}$ is the local electric field caused by the random point defects.

The parameters[60] (all in SI units) in details are $a_1 = 4.29(Coth[\frac{140}{T}] - Coth[\frac{140}{657}]) \times 10^7$, $a_{11} = -2.73 \times 10^8$, $a_{12} = 1.0861 \times 10^9$, $a_{111} = 3.04 \times 10^9$, $a_{112} = -2.73 \times 10^9$, $a_{123} = 1.55 \times 10^{10}$, $a_{1111} = 2.4 \times 10^{10}$, $a_{1112} = 3.73 \times 10^9$, $a_{1122} = 3.34 \times 10^{10}$, $a_{123} = -6.2 \times 10^{10}$, $Q_{11} = 0.13$, $Q_{12} = -0.047$, $Q_{44} = 0.052$, $s_{11} = 5.5 \times 10^{-11}$, $s_{12} = -1.6 \times 10^{-10}$, $s_{44} = 1.3 \times 10^{-9}$. Where s is the Compliance coefficients and Q is the electrostrictive coefficients. A random electric field that obeys the Gaussian distribution $N(0, \triangle)$ was applied, where $\triangle$ is the variance of the Gaussian distribution and can be connected with doping concentration. The simulation scale is 256 dx × 256 dz. The grid scales dx and dz are 1 µm. 9 different grain orientations with the rotations about z direction from −20 to 20 degrees were used to account for the random grain structures. The Fourier method was used for solving the equations. The open circuit electrical boundary condition and the periodic mechanical boundary conditions are adopted in the calculations.

Reporting summary

Further information on research design is available in the Nature Portfolio Reporting Summary linked to this article.

Data availability

The authors declare that the main data supporting the findings of this study are available within the article and its Supplementary Information files. Extra data are available from the corresponding author upon request. Source data are provided with this paper.

References

1. Perdew, J. P. et al. Generalized gradient approximation made simple. *Phys. Rev. Lett.* **77**, 3865–3868 (1996).
2. Waqar, M. et al. Evolution from lead-based to lead-free piezoelectrics: engineering of lattices, domains, boundaries, and defects leading to giant response. *Adv. Mater.* **34**, 2106845 (2022).
3. Kroutvar, M. et al. Optically programmable electron spin memory using semiconductor quantum dots. *Nature* **432**, 81–84 (2004).
4. Liu, H. J. et al. Giant piezoelectricity in oxide thin films with nanopillar structure. *Science* **369**, 292 (2020).
5. Wu, J. et al. Potassium-sodium niobate lead-free piezoelectric materials: past, present, and future of phase boundaries. *Chem. Rev.* **115**, 2559–2595 (2015).
6. Lee, M. H. et al. High-performance lead-free piezoceramics with high curie temperatures. *Adv. Mater.* **27**, 6976 (2015).
7. Wang, X. P. et al. Giant piezoelectricity in potassium-sodium niobate lead-free ceramics. *J. Am. Chem. Soc.* **136**, 2905–2910 (2014).
8. Ahart, M. et al. Origin of morphotropic phase boundaries in ferroelectrics. *Nature* **451**, 545 (2008).
9. Lv, X. et al. Emerging new phase boundary in potassium sodium-niobate based ceramics. *Chem. Soc. Rev.* **49**, 671 (2020).
10. Lin, J. F. et al. Field-induced multiscale polarization configuration transitions of mesentropic lead-free piezoceramics achieving giant energy harvesting performance. *Adv. Funct. Mater.* **33**, 2303965 (2023).
11. Pan, D. et al. Phase structure, microstructure, and piezoelectric properties of potassium-sodium niobate-based lead-free ceramics modified by Ca. *J. Alloys Compd.* **693**, 950 (2017).
12. Li, F. et al. Investigation of new lead free (1-x) KNNS-(x)BKZH piezoceramics with R-O-T phase boundary. *J. Mater. Sci. Mater. Electron.* **28**, 880 (2017).
13. Deng, Y. et al. Structural and electric properties of MnO_2-doped KNN-LT lead-free piezoelectric ceramics. *Crystals* **10**, 1 (2020).
14. Zhang, Y. et al. Effect of three step sintering on piezoelectric properties of KNN-based lead free ceramics. *Chem. Phys. Lett.* **758**, 137906 (2020).
15. Qiao, L. et al. Full characterization for material constants of a promising KNN-based lead-free piezoelectric ceramic. *Ceram. Int.* **46**, 5641–5644 (2020).
16. Xu, K. et al. Superior piezoelectric properties in potassium-sodium niobate lead-free ceramics. *Adv. Mater.* **28**, 8519–8523 (2016).
17. Zheng, T. et al. High-performance potassium sodium niobate piezoceramics for ultrasonic transducer. *Nano Energy* **70**, 104559 (2020).
18. Zheng, T. et al. The structural origin of enhanced piezoelectric performance and stability in lead free ceramics. *Energy Environ. Sci.* **10**, 528–537 (2017).
19. Gao, J. H. et al. Large piezoelectricity in Pb-free $0.96(K_{0.5}Na_{0.5})_{0.95}Li_{0.05}Nb_{0.93}Sb_{0.07}O_3$–$0.04BaZrO_3$ ceramic: a perspective from microstructure. *J. Appl. Phys.* **117**, 084106 (2015).
20. Sun, X. X. et al. Understanding the piezoelectricity of high-performance potassium sodium niobate ceramics from diffused multi-phase coexistence and domain feature. *J. Mater. Chem. A* **7**, 16803 (2019).
21. Zheng, T. et al. Electric field compensation effect driven strain temperature stability enhancement in potassium sodium niobate ceramics. *Acta Mater.* **182**, 1 (2019).
22. Zhang, N. et al. Potassium sodium niobate ceramics with broad phase transition range: temperature-insensitive strain. *Ceram. Inter.* **45**, 24827 (2019).
23. Yao, F. Z. et al. Diffused phase transition boosts thermal stability of high-performance lead-free piezoelectrics. *Adv. Funct. Mater.* **26**, 1217 (2016).
24. Zhang, M. H. et al. High and temperature-insensitive piezoelectric strain in alkali niobate lead-free perovskite. *J. Am. Chem. Soc.* **139**, 3889 (2017).
25. Li, P. et al. High piezoelectricity and stable output in $BaHfO_3$ and $(B_{i0.5}Na_{0.5})ZrO_3$ modified $(K_{0.5}Na_{0.5})(Nb_{0.96}Sb_{0.04})O_3$ textured ceramics. *Acta Mater.* **199**, 542 (2020).
26. Hwang, S. Y. et al. Enhanced thermal stability by short-range ordered ferroelectricity in $K_{0.5}Na_{0.5}NbO_3$-based piezoelectric oxides. *Mater. Horiz.* **10**, 2656 (2023).
27. Wang, K. et al. Temperature-insensitive (K, Na)NbO_3-based lead-free piezoactuator ceramics. *Adv. Funct. Mater.* **23**, 4079 (2013).
28. Song, A. Z. et al. Simultaneous enhancement of piezoelectricity and temperature stability in KNN-based lead-free ceramics via layered distribution of dopants. *Adv. Funct. Mater.* **32**, 2204385 (2022).
29. Xi, K. B. et al. Diffuse multiphase coexistence renders temperature-insensitive lead-free energy-harvesting piezoceramics. *J. Mater. Chem. A* **11**, 3556 (2023).
30. Wang, D. W. et al. Composition and temperature dependence of structure and piezoelectricity in $(1-x)(K_{1-y}Na_y)NbO_3$-$x(Bi_{1/2}Na_{1/2})ZrO_3$ lead-free ceramics. *J. Am. Ceram. Soc.* **100**, 627 (2017).
31. Zheng, T. et al. Compositionally graded KNN-based multilayer composite with excellent piezoelectric temperature stability. *Adv. Mater.* **34**, 2109175 (2022).
32. Messing, G. L. et al. Templated grain growth of textured piezoelectric ceramics. *Crit. Rev. Solid State* **29**, 45 (2004).
33. Kimura, T. Application of texture engineering to piezoelectric ceramics-a review. *J. Ceram. Soc. Jpn.* **114**, 15–25 (2006).
34. Li, P. et al. Ultrahigh piezoelectric properties in textured (K, Na) NbO_3-based lead-free ceramics. *Adv. Mater.* **30**, 1705171 (2018).
35. Lin, J. F. et al. Ultrahigh energy harvesting properties in temperature-insensitive eco-friendly high-performance KNN-based textured ceramics. *J. Mater. Chem. A* **10**, 7978 (2022).
36. Liu, Q. et al. Niobate-based lead-free piezoceramics: a diffused phase transition boundary leading to temperature-insensitive high piezoelectric voltage coefficients. *J. Mater. Chem. C* **6**, 1116 (2017).
37. Lotgering, F. K. Topotactical reactions with ferrimagnetic oxides having hexagonal crystal structures-I. *J. Inorg. Nucl. Chem.* **9**, 113 (1959).

38. Lv, X. et al. Tailoring micro-structure of eco-friendly temperature-insensitive transparent ceramics achieving superior piezoelectricity. *ACS Appl. Mater. Interfaces* **12**, 49795–49804 (2020). **44**.
39. Lin, J. F. et al. Tailoring micro-structure of eco-friendly temperature-insensitive transparent ceramics achieving superior piezo-electricity. *Acta Mater.* **235**, 118061 (2022).
40. Wu, J. G. Perovskite lead-free piezoelectric ceramics. *J. Appl. Phys.* **127**, 190901 (2020).
41. Xing, J. et al. High performance $BiFe_{0.9}Co_{0.1}O_3$ doped KNN-based lead-free ceramics for acoustic energy harvesting perovskite lead-free piezoelectric ceramics. *Nano Energy* **84**, 105900 (2021).
42. Tao, H. et al. Ultrahigh performance in lead-free piezoceramics utilizing a relaxor slush polar state with multiphase coexistence. *J. Am. Chem. Soc.* **141**, 13987 (2019).
43. Li, P. et al. High-performance potassium-sodium niobate lead-free piezoelectric ceramics based on polymorphic phase boundary and crystallographic texture. *Acta Mater.* **165**, 486–495 (2019).
44. Liu, W. F. et al. Large piezoelectric effect in Pb-free ceramics. *Phys. Rev. Lett.* **103**, 257602 (2009).
45. Feng, Y. et al. Defect engineering of lead-free piezoelectrics with high piezoelectric properties and temperature-stability. *ACS Appl. Mater. Interfaces* **8**, 9231–9241 (2016).
46. Watson, B. H. et al. Textured Mn-doped PIN-PMN-PT ceramics: harnessing intrinsic piezoelectricity for high-power transducer applications. *J. Eur. Ceram. Soc.* **41**, 1270–1279 (2021).
47. Yang, W. W. et al. A Study on the relationship between grain size and electrical properties in (K, Na)NbO_3-based lead-free piezo-electric ceramics. *Adv. Electron. Mater.* **5**, 1900570 (2019).
48. Qian, J. et al. Topological vortex domain engineering for high dielectric energy storage performance. *Adv. Energy Mater.* **14**, 2303409 (2024).
49. Jiang, J. et al. Novel lead-free $NaNbO_3$-based relaxor antiferro-electric ceramics with ultrahigh energy storage density and high efficiency. *J. Mater.* **8**, 295–301 (2022).
50. Qian, J. et al. High energy storage performance and large electro-caloric response in $Bi_{0.5}Na_{0.5}TiO_3$-$Ba(Zr_{0.2}Ti_{0.8})O_3$ thin films. *ACS Appl. Mater. Interfaces* **14**, 54012–54020 (2022).
51. Skidmore, T. A. et al. Temperature stability of $([Na_{0.5}K_{0.5}NbO_3]_{0.93}$-$[LiTaO_3]_{0.07})$ lead-free piezoelectric ceramics. *Appl. Phys. Lett.* **94**, 222902 (2009).
52. Zhang, H. B. et al. Temperature-insensitive electric-field-induced strain and enhanced piezoelectric properties of <001> textured (K, Na)NbO3-based lead-free piezoceramics. *Acta Mater.* **156**, 389 (2018).
53. Quan, Y. et al. Large piezoelectric strain with superior thermal stability and excellent fatigue resistance of lead-free potassium sodium niobate-based grain orientation-controlled ceramics. *ACS Appl. Mater. Interfaces* **10**, 10220 (2018).
54. Xu, M. S. et al. Large-area flexible memory arrays of oriented molecular ferroelectric single crystals with nearly saturated polarization. *Small* **18**, 2203882 (2022).
55. Wang, R. P. et al. Temperature stability of lead-free niobate piezoceramics with engineered morphotropic phase boundary. *J. Am. Ceram. Soc.* **98**, 2177–2182 (2015).
56. Acosta, M. et al. Relationship between electromechanical properties and phase diagram in the $Ba(Zr_{0.2}Ti_{0.8})O_3$-$x(Ba_{0.7}Ca_{0.3})TiO_3$ lead-free piezoceramic. *Acta Mater.* **80**, 48–55 (2014).
57. Li, F. et al. Investigation of electromechanical properties and related temperature characteristics in domain-engineered tetragonal $Pb(In_{1/2}Nb_{1/2})O_3$-$Pb(Mg_{1/3}Nb_{2/3})O_3$-$PbTiO_3$ crystals. *J. Am. Ceram. Soc.* **93**, 2731–2734 (2010).
58. Li, J. L. et al. Lead zirconate titanate ceramics with aligned crystallite grains. *Science* **380**, 87–93 (2023).
59. Shi, X. M. et al. Quantitative investigation of polar nanoregion size effects in relaxor ferroelectrics. *Acta Mater.* **237**, 118147 (2022).
60. Pohlmann, H. et al. A thermodynamic potential and the temperature-composition phase diagram for single-crystalline $K_{1-x}Na_xNbO_3$ ($0 \le x \le 0.5$). *Appl. Phys. Lett.* **110**, 102906 (2017).

Acknowledgements

This work was supported by the National Natural Science Foundation of China under Grant (Nos. 52032007, 51772211, and 52172128) and the National Key R&D Program of China (2021YFB3201100). We thank the Instrument Analysis Center of Xi'an Jiaotong University for assistance with electron microscopy characterization.

Author contributions

Conceptualization: X.L.H., L.J.F. Data curation: X.L.H. Methodology: X.L.H., L.J.F., S.X.M., F.Z.Q., L.P. Investigation: X.L.H. Funding acquisition: Z.J.W., S.B., W.H.J. Project administration: X.L.H., L.J.F., Y.Y.X., Z.Z.H., S.X.M., G.G.L., Q.J., S.C., L.G.H., W.S.M., Z.Y. Supervision: S.B., W.H.J., L.F., H.H.B., Ding X.D., S.J., Z.J.W. Writing - original draft: X.L.H. Writing - review & editing: X.L.H., L.J.F., Y.Y.X., S.X.M., W.H.J., Z.J.W.

Competing interests

The authors declare no competing interests.

Additional information

Supplementary information The online version contains supplementary material available at https://doi.org/10.1038/s41467-024-53437-5.

Correspondence and requests for materials should be addressed to Bo Shen, Haijun Wu, Houbing Huang or Jiwei Zhai.

Peer review information *Nature Communications* thanks Jung Woo Lee, Yuho Min, C. Siva, and the other anonymous reviewer(s) for their contribution to the peer review of this work. A peer review file is available.